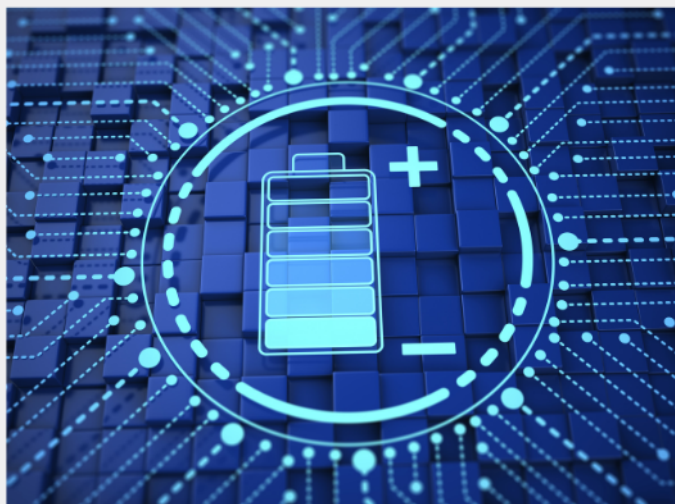




Exploring the possibilities of increasing energy density and efficiency in rechargeable batteries

Download this complimentary article collection



The exponential rise in the need for better, more efficient power sources has sparked an incredible amount of research into batteries. A primary focus of research has been increasing the energy density of batteries, as it allows for lighter, more portable storage of energy. Lithium-ion batteries, for example, have a much higher energy density than conventional lead-acid batteries and can be used for various purposes, such as in electric vehicles.

This article collection provides a comprehensive list of references for new methods and technologies for increasing the energy density of batteries.



WILEY

Magnetic Nanoislands in a Morphotropic Cobaltite Matrix

Shengru Chen, Dongke Rong, Yan-Xing Shang, Miming Cai, Xinyan Li, Qinghua Zhang, Shuai Xu, Yue Xu, Hanbin Gao, Haitao Hong, Ting Cui, Qiao Jin, Jia-Ou Wang, Lin Gu, Qiang Zheng, Can Wang, Jinxing Zhang, Gang-Qin Liu, Kui-Juan Jin,* and Er-Jia Guo*

High-density magnetic memories are essential components for spintronics, quantum computing, and energy-efficient electronics. Miniaturization of magnetic storage units requires reduced dimensionality and magnetic domain stability at the nanoscale. However, inducing magnetic order and selectively tuning spin-orbital coupling at specific locations is challenging. Here, an unprecedented approach is demonstrated to construct switchable magnetic nanoislands in a nonmagnetic matrix based on cobaltite homostructures. The magnetic and electronic states are laterally modified by epitaxial strain, which is regionally controlled by freestanding membranes. Tensile-strained cobaltite layers exhibit ferromagnetic properties, while compressively strained cobaltite layers exhibit a small magnetic response to applied fields. The minimum size of magnetic nanoislands reaches ≈ 35 nm in diameter, suggesting the highest possible areal density can reach up to ≈ 400 Gbit/in². This methodology provides an ideal platform for precisely controlled read/write schemes and enables scalable and patterned memories on silicon and flexible supports for various applications.

nanodomains.^[2,3] However, superparamagnetic effects in magnetic materials limit the minimum domain size.^[4,5] Patterning continuous magnetic media composed of highly coupled magnetic grains into discrete single nanostructures has been proposed. Using direct-write e-beam lithography, magnetic circular dot arrays with an areal density of ≈ 65 Gbit/in² have been commercialized.^[6] However, they have reached not only the device fabrication limit, but also the characterization limit of individual elements. Therefore, advanced materials and evolutionary fabrication processes are required to further reduce the periodicity of magnetic units to < 25 nm to produce patterned media with enhanced areal density (> 1 Tbit/in²).^[7]

Magnetic oxides are ideal candidates for fabricating memory devices owing to their chemical stability, strong magnetic

anisotropy, and relatively large coercivity. Heavy orbital hybridization between transition metal ions and oxygen ions results in strong correlations among different degrees of freedom.^[8] Previous studies demonstrated the manipulation of magnetic anisotropy owing to oxygen octahedral interconnection at interfaces.^[9–11] For instance, the octahedral rotation in manganese layers is steeply suppressed by inserting a single-unit-cell-thick SrTiO₃ layer between films and substrates, resulting in the rotation of the in-plane magnetic easy axis.^[9,10] Alternatively, the control of structural parameters can be achieved by capping an

1. Introduction

Magnetic storage units are the smallest patterns of magnetization in magnetizable materials used for data storage. The digital information in the binary form (0 or 1 bit) can be accessed or processed from a magnetic head.^[1] To increase the capacity of magnetic storage, the dimensionality of basic elements must be reduced while preserving the stability of magnetic

S. Chen, D. Rong, Y.-X. Shang, X. Li, Q. Zhang, S. Xu, Y. Xu, H. Hong, T. Cui, Q. Jin, C. Wang, G.-Q. Liu, K.-J. Jin, E.-J. Guo
Beijing National Laboratory for Condensed Matter Physics and Institute of Physics, Chinese Academy of Sciences
Beijing 100190, China
E-mail: kjjin@iphy.ac.cn; ejguo@iphy.ac.cn

S. Chen, X. Li, S. Xu, Y. Xu, H. Hong, T. Cui, K.-J. Jin, E.-J. Guo
School of Physical Science
University of Chinese Academy of Sciences
Beijing 101408, China

M. Cai, J. Zhang
Department of Physics
Beijing Normal University
Beijing 100875, China

H. Gao, Q. Zheng
CAS Key Laboratory of Standardization and Measurement for Nanotechnology
CAS Center for Excellence in Nanoscience
National Centre for Nanoscience and Technology
Beijing 100190, China

J.-O. Wang
National Center for Electron Microscopy in Beijing and School of Materials Science and Engineering
Tsinghua University
Beijing 100084, China

L. Gu
Institute of High Energy Physics, Chinese Academy of Sciences
Beijing 100049, China

C. Wang, G.-Q. Liu, K.-J. Jin, E.-J. Guo
Songshan Lake Materials Laboratory
Dongguan, Guangdong 523808, China

 The ORCID identification number(s) for the author(s) of this article can be found under <https://doi.org/10.1002/adfm.202302936>

DOI: 10.1002/adfm.202302936

ultrathin layer with dissimilar symmetry.^[11] An enhanced magnetic phase transition temperature and perpendicular magnetic anisotropy in ultrathin ferromagnetic oxides were observed after interfacial modifications.^[12] Furthermore, using lithographic patterning, we locally controlled the magnetic properties of oxide heterostructures,^[13] expanding possibilities for developing memory devices at the nanoscale. Despite the control of magnetic anisotropy by oxide interface engineering, the crosstalk between nearby magnetic domains in thin films remains unavoidable. One strategy to break centrosymmetry in continuous 2D thin films is to fabricate magnetizable domains in a nonmagnetic matrix using single materials. It requires magnetic materials that are highly sensitive to structural distortions so that their magnetic and electronic properties can be directly tuned.

Recent investigations revealed that the magnetic states of ferroelastic LaCoO₃ (LCO) are actively correlated to epitaxial strain.^[14] Small lattice distortions, such as deformations and oxygen octahedral tilts (or rotations) modify the balance between crystal field splitting (Δ_{cf}) and intraatomic exchange interaction (Δ_{ex}); thus, the spin states of Co ions are reversibly switched.^[15] Generally, tensile strain increases the population of higher-spin-state Co³⁺ ions, resulting in a robust ferromagnetic state, whereas in-plane compression promotes lower-spin-state transition; as a result, long-range magnetic ordering cannot be formed in compressively strained LCO films.^[16] Therefore, LCO has been recognized as a promising route for controlling magnetic states using strain engineering. Typically, for modifying the strain states of epitaxial films, changing substrate materials, or introducing buffer layers with different compositions was reported.^[17,18] However, this regulates the in-plane strain states, crystalline orientations, or rotation patterns of the films once a substrate is chosen. It is challenging to modify electronic and magnetic states regionally along the film plane. Recently, Wu et al. and Chen et al. reported the growth of ferroic oxide thin films with laterally tunable strains and orientations using acid-soluble manganite layers and water-soluble sacrificial layers, respectively.^[19,20] In both cases, the original substrates, and suspended freestanding membranes served as independent building blocks for the epitaxial growth of functional oxides. Here, we report the construction of cobaltite homostructures using single crystalline substrates that are partially modified by freestanding membranes. The magnetic and electronic states of each layer can be unprecedentedly tuned by misfit strains. Furthermore, we fabricated ferromagnetic nanoislands with diameters of tens of nanometers in nonmagnetic media. The methodology described in present work implies a potential to develop ultrahigh-density magnetic storage if one chooses suitable room-temperature ferromagnets.

2. Results

2.1. Fabrication of Lateral Homostructure Using Ultrathin Freestanding Membranes

We first deposited water-soluble sacrificial Sr₃Al₂O₆ (SAO) layers (≈ 30 nm)^[14] and SrTiO₃ (STO) layers (≈ 3 nm) subsequently on (001)-oriented (LaAlO₃)_{0.3}-(Sr₂AlTaO₆)_{0.7} (LSAT) single-crystalline substrates using pulsed laser deposition (PLD).

The ultrathin STO membrane was thermally transferred on LaAlO₃ (LAO) after delamination from LSAT substrates (see Experimental Section). The freestanding STO (FS-STO) membranes maintained their original shape and high crystallinity at the millimeter scale. **Figure 1a** shows the schematic of a grain boundary area, in which contains both LCO_C (compressively strained LCO by LAO) and LCO_T (tensile strained LCO by FS-STO) regions in a single LCO hybrid homostructure. The strain state of LCO_C and LCO_T are quantitatively determined by XRD θ - 2θ scans and reciprocal space mappings (RSM) (**Figure 1b,c**). The LCO_C exhibits a compressive strain of $\approx -0.52\%$, resulting in $\approx 0.7\%$ elongation along the out-of-plane direction. We found that the in-plane lattice constant of FS-STO reduces to 3.874 ± 0.015 Å, while its out-of-plane lattice constant increases to 3.920 ± 0.008 Å. The lattice parameters of FS-STO membrane are different from those of bulk STO (3.905 Å). We believe that the in-plane compressive strain presents within the ultrathin FS-STO comes from the lattice interaction with the above relatively thick LCO_T layers. Thus, the in-plane strain of LCO_T reduces from 2.5% (on STO substrates) to 1.68% (on FS-STO membranes).

Microscopic structural analysis was examined by cross-sectional high-angle annular dark field (HAADF) imaging via scanning transmission electron microscopy (STEM) (**Figure 1d**; **Figure S1**, Supporting Information). A representative HAADF-STEM image from a grain boundary (GB) region in LCO hybrid homostructures shows that the LCO_C and LCO_T heterointerfaces are atomically sharp. The GB is nearly invisible due to the fairly small lattice difference. We could observe a clear boundary (marked in white dashed lines) within LCO layers $\approx 45^\circ$ with respect to the interfaces after calculating the atomic distance between A-site ions along in-plane (**Figure 1e**) and out-of-plane (**Figure 1f**) directions. LCO_C (LCO_T) layers were coherently grown on LAO substrates (FS-STO membranes) with nearly identical in-plane lattice constants. The out-of-plane lattice constant of LCO_T was considerably smaller than that of LCO_C, consistent with XRD results. The FS-STO membranes with a thickness of ≈ 7 unit cells uniformly covered LAO substrates with an extremely narrow gap (≈ 1 nm). Different from epitaxial thin films, the chemically unbonded FS-STO membranes did not involve misfit strain resulting from LAO substrates, allowing the suspended LCO films to follow the strain and orientation of FS-STO membranes (**Figure S2**, Supporting Information). We observed mainly periodic dark stripe patterns perpendicular to the interface in LCO_T while these superstructures were absent in LCO_C. These results are in excellent agreement with previous observations.^[15] Since the degree of tensile strain reduces in LCO_T, relatively fewer stripes appear compared to the tensile-strained LCO films sandwiched between STO in our previous work.^[16] Notably, the dark stripes exist only in the regions close to FS-STO membranes, indicating that the tensile strain partially relaxes with increasing LCO_T film thickness. Furthermore, we performed optical second-harmonic generation (SHG) measurements on LCO_C and LCO_T independently. As indicated in **Figure 1g** and **Figure S3** (Supporting Information), LCO_T fit the point group *P4mm*, while LCO_C belong to the point group *m*, suggesting that these layers exhibit different crystallographic symmetries under distinct misfit strains.

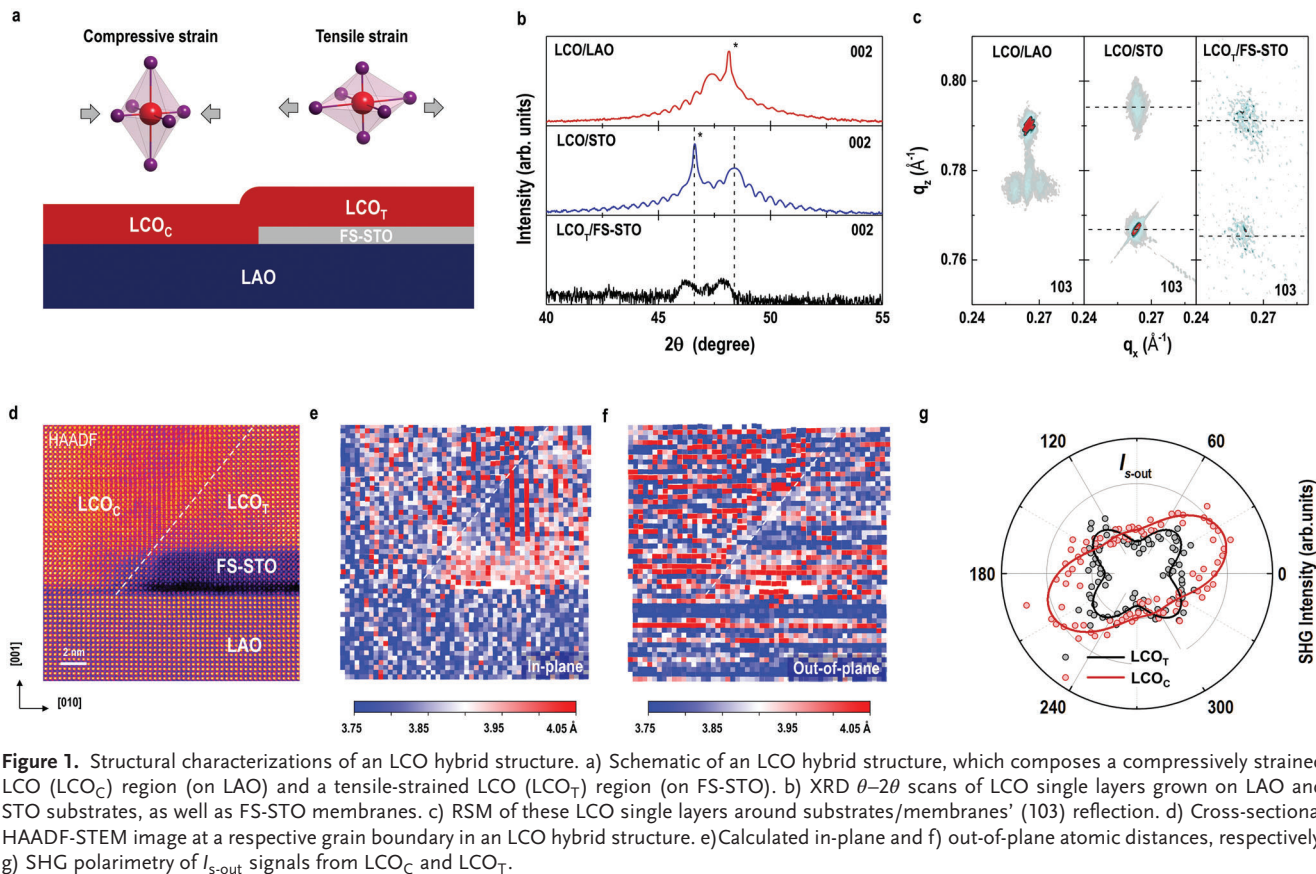


Figure 1. Structural characterizations of an LCO hybrid structure. a) Schematic of an LCO hybrid structure, which composes a compressively strained LCO (LCO_C) region (on LAO) and a tensile-strained LCO (LCO_T) region (on FS-STO). b) XRD θ - 2θ scans of LCO single layers grown on LAO and STO substrates, as well as FS-STO membranes' (103) reflection. c) RSM of these LCO single layers around substrates/membranes' (103) reflection. d) Cross-sectional HAADF-STEM image at a respective grain boundary in an LCO hybrid structure. e) Calculated in-plane and f) out-of-plane atomic distances, respectively. g) SHG polarimetry of $I_{s\text{-out}}$ signals from LCO_C and LCO_T .

2.2. Unique Magnetic Ground States in Different Strained Cobaltites

The observed structural modification is strongly related to macroscopic magnetic properties in LCO hybrid homostructures. We performed magnetic measurements on LCO hybrid homostructures, LCO single-crystalline films grown on LAO and STO substrates. As shown in Figure 2a,b, the magnetization (M) exhibits a square-like hysteresis loop as a function of field and a sharp transition with increasing temperature, corroborating the ferromagnetic order in LCO hybrid homostructures. The M - H curves of LCO hybrid homostructures exhibit a small kink in the low-field region. This anomaly is attributed to the paramagnetic (PM) signal from compressively strained LCO films on LAO.^[17] Considering the area ratio ($\text{LCO}_C:\text{LCO}_T \approx 60:40$), the saturation M and field dependency of LCO hybrid homostructures are almost identical to those of LCO single layer on STO (Figure S4, Supporting Information). The distinct magnetic properties of LCO_C and LCO_T were revealed by performing nanodiamond (ND) nitrogen-vacancy (NV) magnetometry measurements.^[18] NV magnetometry was performed at zero magnetic fields and switchable temperatures ranging from 6 to 120 K. By recording optical detected magnetic resonance (ODMR) spectra of the numbers of NV centers in a single ND, we calculated the projection of the magnetic stray field along the NV axis due to the energy splitting ($2\gamma B$) in the presence of weak magnetic perturbation (B). Since NDs were dispersed on the sample surface, we measured the ODMR spec-

trum from either LCO_T or LCO_C at different locations independently. Figure 2c shows the ODMR spectra of a single ND on LCO_T (left panels) and LCO_C (right panels) at various temperatures. At low temperatures, the splitting between two resonance peaks from LCO_T was large, and it reduced gradually with increasing temperature. However, the energy splitting from LCO_C maintained a small, but fixed value as the temperature increasing. We calculated $2\gamma B$ by subtracting two resonant peak frequencies and summarized these values as open symbols in Figure 2b, although NV magnetometry cannot obtain the exact net moment of individual layers because the magnitude of $2\gamma B$ depends on the number of NVs in a single ND, proximity distance, and magnetic homogeneity. The temperature-dependent $2\gamma B$ yields the estimated Curie temperature (T_C) of LCO_T (≈ 80 K), which agreed with that obtained from SQUID measurements. $2\gamma B$ obtained from LCO_C remained nearly constant at all temperatures, suggesting that M weakly depended on temperature when LCO films were compressively strained. The discrepancies between $2\gamma B$ - T and M - T curves at low temperatures indicate additional PM contributions from substrates and FS-STO membranes. The SQUID measures the total M from an entire sample, while NV magnetometry is insensitive to PM signals originating from the layers/substrates under LCO_C and LCO_T , making it advantageous to apply NV magnetometry to measure magnetic properties in different regions.

Field-dependent magnetic force microscopy (MFM) measurements were conducted at 6 K. Figure 2d,e shows the MFM im-

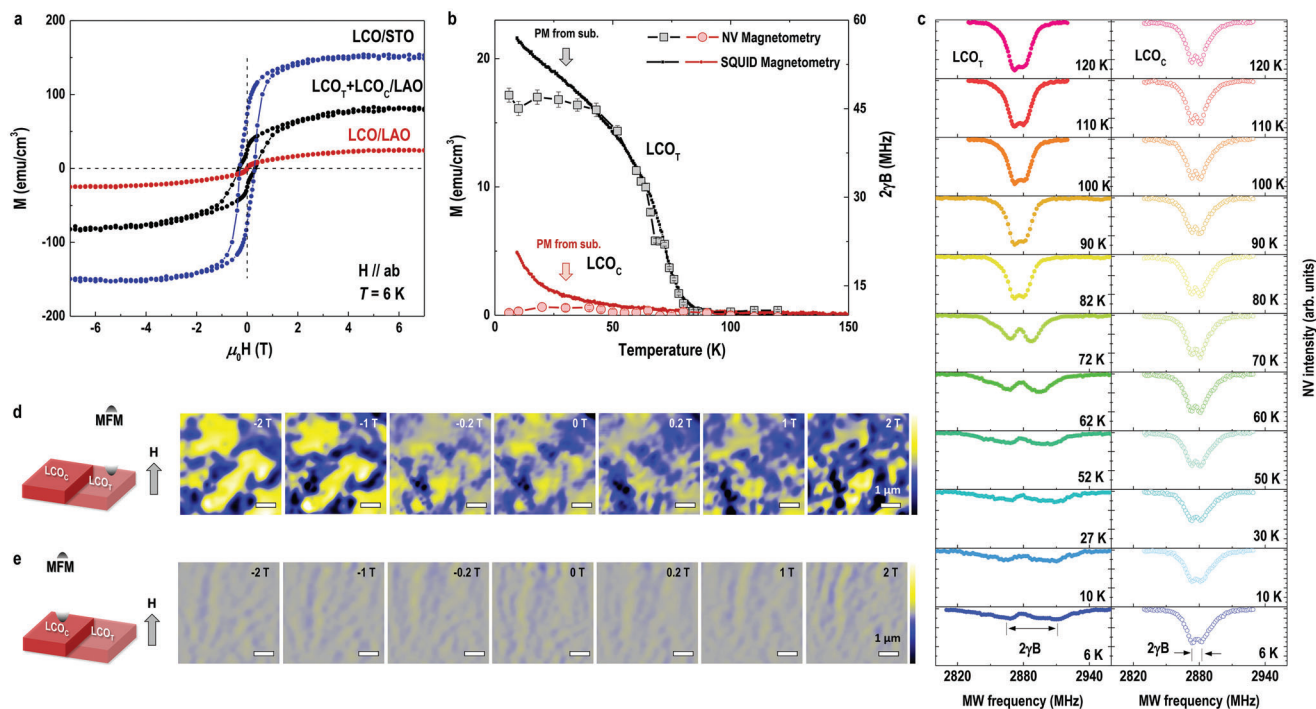


Figure 2. Magnetically distinct regions in an LCO hybrid structure. a) M – H hysteresis loops and b) M – T curves of an LCO (on LAO) LCO (on STO) single layers and an LCO hybrid homostructure. M – H loops were recorded at 6 K. M – T curves were measured during sample warm-up under an in-plane field of 1 kOe. c) Zero-field ODMR spectra of NV centers dispersed on the LCO hybrid structure. ODMR spectra were collected from LCO_T (left) and LCO_C (right), respectively. $2\gamma B$ were subtracted and plotted in (b) as open symbols. MFM images taken from d) LCO_T and e) LCO_C at 6 K, respectively, under different external out-of-plane magnetic fields from -2 to 2 T. The scale bar is $1 \mu\text{m}$.

ages of LCO_T and LCO_C collected when the out-of-plane magnetic fields switched between -2 and 2 T, respectively. At -2 T, the LCO_T layers contained static multiple magnetic domains with reversed polarity. As the magnetic field increased from -2 to 2 T, magnetic domains (yellow) in LCO_T shrank and showed reversed polarity (blue). These results demonstrate the ferromagnetic character of LCO_T . Please note that the maximum applied field cannot not saturate the out-of-plane magnetic domains, thus the observed MFM image does not show a relatively uniform single domain structure. On the contrary, LCO_C did not show magnetic phase contrast, and these domains barely changed with applied fields, suggesting that LCO_C are nonferromagnetic. These results are consistent with SQUID and NV magnetometry measurements. Microscopic magnetic imaging indicates that the lateral magnetic ground states in LCO hybrid homostructures strongly depend on epitaxial strain.

2.3. Electronic States Modified by Freestanding Membranes

The correlation between strain and the electronic states of valence electrons in LCO hybrid homostructures was revealed by performing element-specific X-ray absorption spectroscopy (XAS) measurements at room temperature. **Figure 3a** shows the XAS results at O K -edges for LCO_C and LCO_T layers. The shadow region centered at ≈ 530 eV represents the excitation of electrons from O $1s$ to the Co $3d$ –O $2p$ hybridization states. Both XAS curves agree well with the features of XAS at O K -edges for bulk

$\text{LaCo}^{3+}\text{O}_3$ (Figure S5, Supporting Information).^[26] Meanwhile, the XAS results at Co L -edges showed strong peaks at ≈ 780 eV (L_3) and ≈ 795 eV (L_2) corresponding to the excitations of electrons from the $2p$ core levels to the $3d$ unoccupied states, consistent with the peak positions of Co^{3+} ions.^[27] These results indicate that the valence state of Co ions ($+3$) was maintained regardless of the film strain. Some layers did not show significant numbers of oxygen vacancies, which may influence the magnetization of LCO layers. Orbital occupancy in different regions of the LCO hybrid homostructure was further characterized by X-ray linear dichroism (XLD) using linearly polarized X-ray beams with variable incident angles, as shown in Figure 3b,c. When the incident angle is 90° , one anticipates that the absorption of X-rays (I_{90°) arises entirely from in-plane orbitals ($d_{x^2-y^2}$). When the incident angle switches to 30° with respect to the surface plane, the XAS signals (I_{30°) contain both $d_{x^2-y^2}$ and $d_{3z^2-r^2}$ orbital information. Comparing the difference in the peak energy between I_{90° and I_{30° (Figure 3d,e), we noticed that the LCO_T layer under tensile strain had a lower peak energy of the $d_{x^2-y^2}$ orbital compared to that of the $d_{3z^2-r^2}$ orbital, while the LCO_C layer showed the opposite effect. We calculated the nominal XLD value by subtracting I_{30° from I_{90° for both LCO_T and LCO_C layers (Figure 3f,g). The XLD value is negative for the tensile-strained LCO_T layer, suggesting higher electron occupancy in $d_{x^2-y^2}$ orbitals, whereas the LCO_C layer showed a positive XLD value, indicating that electrons preferentially occupy the $d_{3z^2-r^2}$ orbital instead. The difference in the electron occupancy determines the spin states of Co^{3+} ions under different strain states. Consequently, the spin states of Co

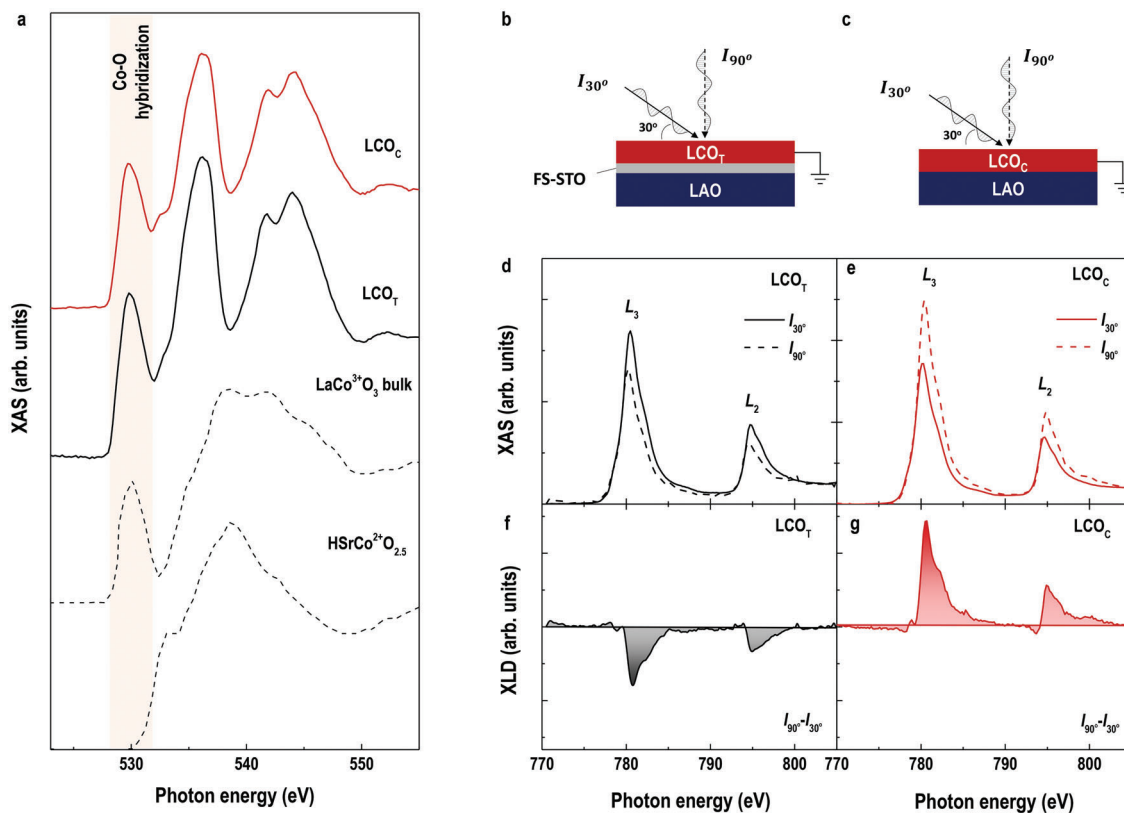


Figure 3. Laterally separated spin states in an LCO hybrid structure. a) XAS at O *K*-edges collected from LCO_C and LCO_T. The dashed lines show the reference data from bulk LaCo³⁺O₃ and H5rCo²⁺O_{2.5} films. Schematics of measured geometries in b) LCO_C and c) LCO_T, respectively. XAS were collected using the TEY mode at room temperature. XAS at Co *L*-edges from d) LCO_C and e) LCO_T, respectively. The calculated nominal XLD ($= I_{90^\circ} - I_{30^\circ}$) of f) LCO_C and g) LCO_T, respectively.

ions change from high spin states in LCO_T to low spin states in LCO_C. The systematic XAS results provide solid evidence of the strain-mediated magnetic states of LCO hybrid homostructures, which agreed well with earlier magnetization characterizations.

2.4. Fabrication of Magnetic Domains Using Ultrasmall Freestanding Nanoislands

We aimed to shrink ferromagnetic LCO_T domains within a non-ferromagnetic LCO_C matrix by fabricating FS-STO nanoislands using PLD through ultrathin anodic aluminum oxide (AAO) masks (see Experimental Section). This fabrication method has been widely used in the past for creating nanoscale capacitors and ferroelectric domains.^[28–31] Previous work has demonstrated that the fabrication of nanodomains with a size >100 nm is relatively easy to achieve periodic arrays,^[30,31] while obtaining unbroken arrays for nanodomains with a size <50 nm is a challenge. The fabrication procedure of LCO nanoislands is summarized in Figure 4a, and the structures of the AAO masks and FS-STO nanoislands were characterized using scanning electron microscopy (SEM), as shown in Figure 4b,c and Figure S6 (Supporting Information). An array of nanoislands was formed from the AAO mask, resulting in self-ordered domain patterns. We analyzed the averaged diameters of AAO nanopores and the

resulting nanoislands, which are ≈40 and 35 nm, respectively (Figure 4d,e). The slightly smaller size of the nanoislands may be attributed to the shadow effect during the PLD deposition.^[32,33] The averaged distance between each nanoislands (edge to edge) is ≈20 nm. In Figure 4f and Figure S7 (Supporting Information), we show a STEM image of an individual LCO_T nanodomain with a diameter of ≈35 nm. The strain distributions within an LCO single nanodomain along the in-plane and out-of-plane directions are analyzed in detail (Figure 4g,h). The LCO_T layers exhibited a larger in-plane lattice constant than LCO_C layers, whereas the out-of-plane lattice constant of LCO_T decreased slightly due to the tensile strain. Thus, the strain modulation in LCO_T nanoislands is still valid at the nanoscale, suggesting that large-area control of ordered nanoislands could have various applications. Figure 4i depicts a schematic of the proposed crossbar device structure with a vertical/horizontal write and readout geometry. The self-designed array of individually addressable ferromagnetic nanodomains offers several advantages. As the individual memory elements storing the bits of the data are physically separated. Thus, the electrical readout through the crossbar structure is localized, thereby further reducing crosstalk. Additionally, the results demonstrate that using an ultrathin AAO membrane as a lift-off mask enables the generation of arrays of ferromagnetic nanoislands that serve as building blocks for memory applications. Considering the size of nanoislands and the dis-

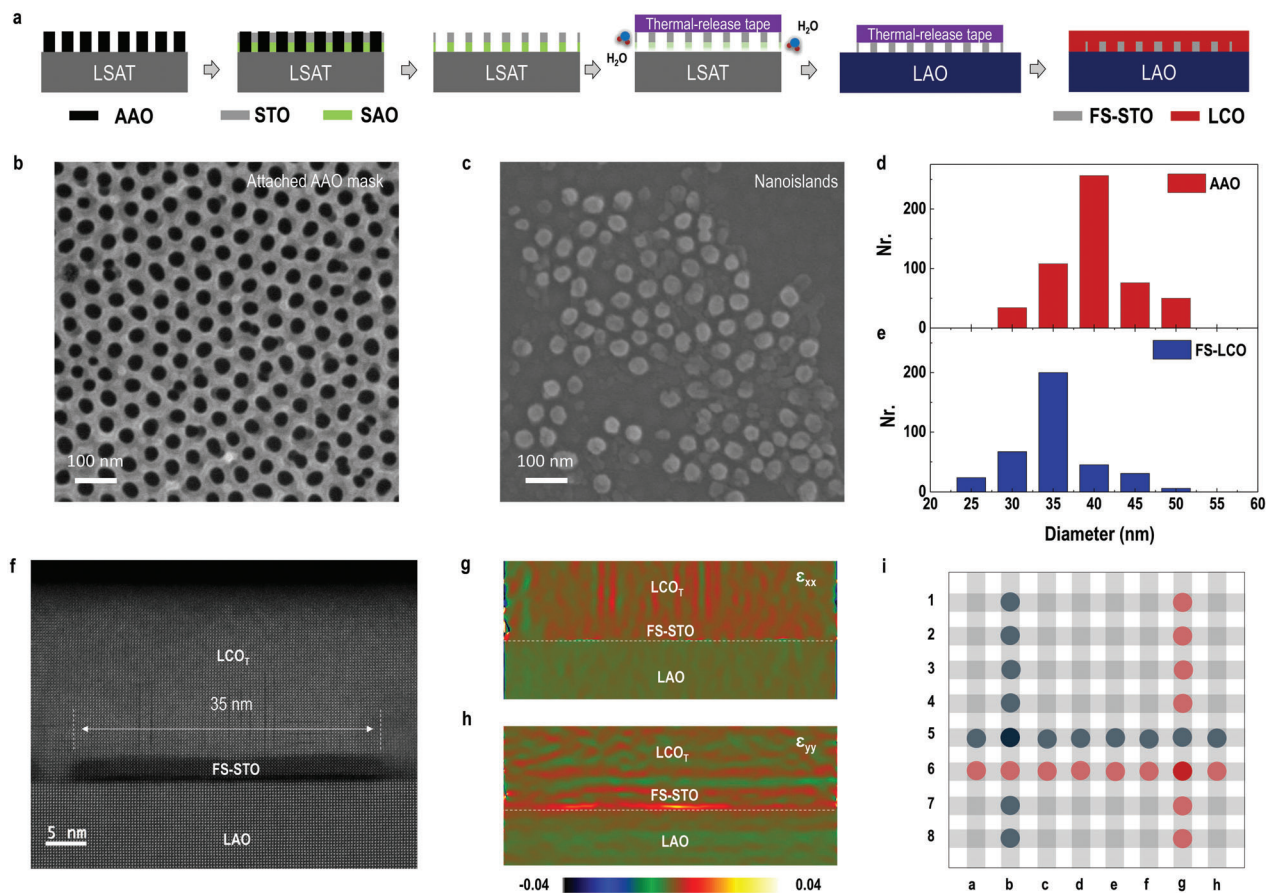


Figure 4. Ferromagnetic nanoislands in a nonmagnetic matrix. a) Fabrication process of nanoislands. SEM images of b) AAO mask and c) FS-STO nanoislands. Histograms of the diameters of d) AAO nanopores and e) nanoislands within $1 \mu\text{m}^2$, respectively. f) Cross-sectional HAADF-STEM image of a single LCO_T nanodomain in the LCO_C matrix. g) In-plane strain (ϵ_{xx}) and h) out-of-plane strain (ϵ_{yy}) distributions at the interface, respectively. i) Schematic of programmatically addressable magnetic nanoislands.

tance between these nanoislands, we estimated an areal density reaches $\approx 400 \text{ Gbit/in}^2$. We believe a higher storage density is possible by further reducing the size of nanoislands and the distance between nanoislands. However, the experimentally achievable lower limit for the nanodomain size is unclear, as it depends on growth conditions and nanofabrication techniques. We could imagine that it is challenge to avoid severe crosstalk between nearby bits when these nanoislands become physically closer. Many technique issues remain to be solved in future. Moreover, the size of nanodomains would not significantly influence magnetic properties because the film thickness along the growth direction can be precisely controlled to maintain its long-range spin ordering.

2.5. Universal Compatible with Both CMOS and Flexible Electronics

Finally, we demonstrate that ferromagnetic nanodomains in cobaltite homostructures can be integrated into silicon-based CMOS technology. Using the same strategy, FS-STO membranes were transferred onto silicon (Figure 5a). The LCO_T layers grown on FS-STO membranes were highly epitaxial and maintained

a tensile strain of $\approx 1.6\%$. The epitaxial strain of LCO_T layers was slightly smaller than that of LCO_T layers directly grown on STO substrates (Figure 5b). We observed a similar orbital polarization in LCO_T layers independent of the target substrate (Figure S8, Supporting Information), yielding identical strain effects on epitaxial LCO_T layers. These LCO_T layers showed a typical ferromagnetic character with a clear magnetic phase transition. T_C increased by $\approx 5 \text{ K}$ compared to the T_C of LCO_T single layers (Figure 5c). Moreover, the M_S of LCO_T layers on FS-STO membranes reached $\approx 217 \text{ emu/cm}^3$ ($\approx 1.44 \mu_B/\text{Co}$), which is $\approx 50\%$ larger than that of LCO_T single layers. Enhanced M_S in LCO_T layers can be attributed to the reduced tensile strain. Previously, it was reported that the M_S of LCO films grown on LSAT was larger than that of LCO films grown on STO.^[16,34] In both cases, the Co–O bond length ($d_{\text{Co-O}}$) was stretched, and the Co–O–Co bonding angle ($\beta_{\text{Co-O-Co}}$) remained at 180° . Slightly decreased tensile strain reduces $d_{\text{Co-O}}$. In this case, $(\Delta_{\text{cf}} - W/2) \propto (1/d_{\text{Co-O}}^5 - 1/d_{\text{Co-O}}^{3.5})$ continuously increases, leading to a strong overlap between the t_{2g} and e_g bands. Valence electrons depopulate the t_{2g} band in favor of $d_{x^2-y^2}$ orbitals; thus, Co^{3+} ions prefer high spin states and larger M_S in LCO_T layers on FS-STO membranes. Surprisingly, we observed a double hysteresis in $M-H$ loops with a small coercive field of $\approx 800 \text{ Oe}$.

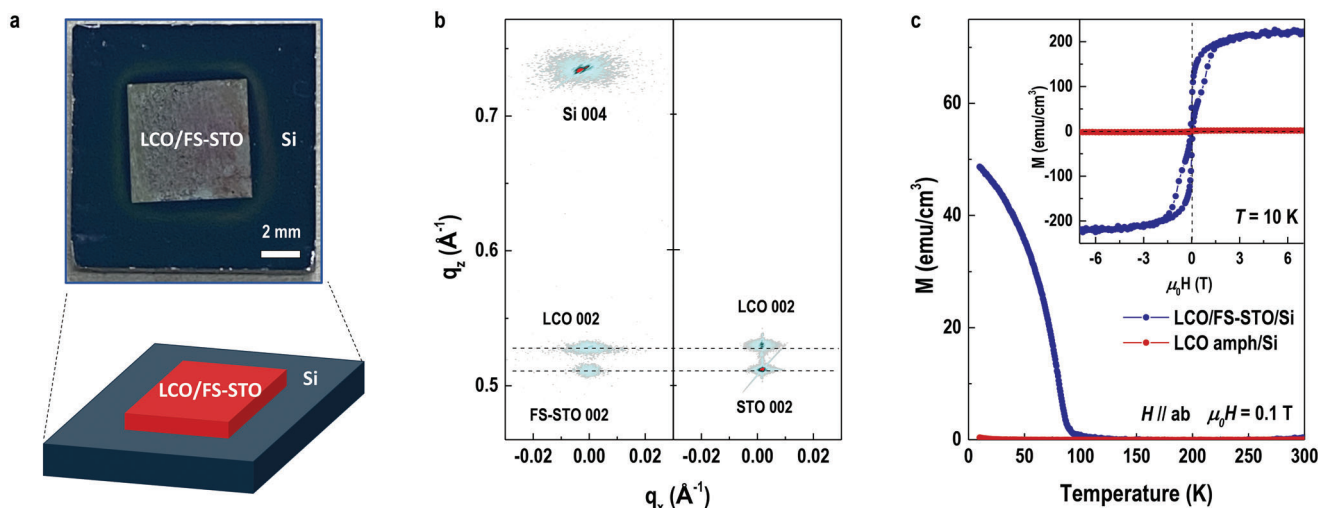


Figure 5. Intergration freestanding membranes with silicon. a) Schematic and optical photograph of an LCO_T/FS-STO on silicon. b) Direct comparison of RSMs between an LCO_T/FS-STO membrane on silicon and an LCO on STO around substrates' (00L) reflections. c) M - T curve of an LCO_T/FS-STO on silicon and an LCO amorphous (a-LCO) layer on silicon under an in-plane field of 1 kOe. The inset shows its M - H loops at 10 K.

We believe the change in field-dependent magnetization is attributed to strain relaxation with increasing LCO_T layer thickness. In addition, we measured the magnetic properties of the FS-LCO membrane and LCO amorphous layers grown directly on silicon (Figure S9, Supporting Information). Both samples were nonferromagnetic, similar to their bulk form, revealing the influence of epitaxial strain on the stabilization of long-range spin ordering. The methodology described in the present work can be applied to arbitrary substrates, such as amorphous glass and α -Al₂O₃ (Figure S10, Supporting Information). LCO_T layers maintained their high crystallinity and orientation, similar to the buffered ultrathin membranes.

The methodology described in the present work not only limit to the magnetic cobaltites, but also could extends to other ferromagnetic oxides or ferroelectric oxides. For the device applications, one needs to choose magnetic materials that exhibit tunable magnetic states at the room-temperature, for instance La_{1-x}Sr_xMnO₃,^[35] CoFe₂O₄,^[36] and YIG.^[37] Furthermore, this work also implies the design of a functional grain boundary (GB) with dissimilar orientation and strain laterally. Previous work demonstrates the formation of charged domain walls in multiferroics (for instance, BiFeO₃),^[38-40] exhibiting a quasi-2D conducting path that coupled to polarization switching. In these cases, the atomically thin GB may serve as another type of information storage media with remarkably high density in the film plane. In addition, this work enables the replacement of ultrathin dielectric STO membranes with other multifunctional (superconducting, ferroelectric, or photoelectric) oxide membranes. The stacking of these correlated oxide membranes with controllable twist angle, stacking order, and periodicity may provide a vigorous platform for both fundamental research and applied sciences.

3. Conclusion

This work demonstrates the construction of ferromagnetic nanoislands in a nonmagnetic cobaltite matrix. Epitaxial strain was induced using freestanding membranes or substrates to lat-

erally modify the electronic and magnetic states of cobaltite homostructures. Magnetic contrast was observed at the nanoscale, and ultrathin small size nanodomains were successfully fabricated. These results suggest the potential for achieving ultrahigh areal density for data storage by choosing appropriate room-temperature magnetic materials. Furthermore, the generic method presented in this study can be applied to both silicon and flexible substrates, paving the way for the fabrication of nanoscale magnetic elements using various thin film epitaxy techniques.

4. Experimental Section

Sample Synthesis and X-Ray Based Structural Characterizations: Pulsed laser deposition (PLD) technique was used to fabricate oxide thin films and heterostructures in the present work. It was first fabricated the water-soluble Sr₃Al₂O₆ (SAO) layer with thickness ≈ 30 nm on (001)-oriented (LaAlO₃)_{0.3}-(Sr₂AlTaO₆)_{0.7} (LSAT) substrates with size of 25 mm² (Hefei Kejing Mater. Tech. Co. Ltd). Subsequently, a 7-unit-cells-thick SrTiO₃ (STO) ultrathin layer was deposited on SAO layers. We kept the substrate's temperature was 750°C and laser density was ≈ 1.5 J/cm² for both layers. However, the oxygen partial pressure maintained 35 mTorr for SAO and increased to 100 mTorr for STO capping layers in order to achieve the best sample quality. After the sample growth, a thermal-release tape was firmly pressed on the as-grown samples and then immersed into deionized water at room temperature. The ultrathin freestanding (FS) STO membranes was adhered on the tape after the SAO fully dissolved. Then, the FS-STO membranes were carefully transferred on LaAlO₃ (LAO) substrates or other (glass, α -Al₂O₃, and silicon) supports using standard heating release process. Finally, LCO films with a thickness ≈ 20 nm were fabricated on the modified substrates at the substrate's temperature of 700°C, laser density of ≈ 1 J/cm², and oxygen partially pressure of 100 mTorr. For the sample quality control purpose, LCO single films on STO and LAO substrates for direct comparison were fabricated. After the growth, the LCO samples were cooled down to room temperature under an annealing oxygen pressure of 100 Torr in order to largely remove the potential impacts from oxygen vacancies. The crystallographic analysis, including XRD θ - 2θ scans and reciprocal space mapping (RSM), were carried out using synchrotron-based diffractometer and lab-based Panalytical X'Pert3 MRD diffractometer. The LCO film thickness (22 ± 1 nm) was obtained from fitting X-ray reflectivity curves using GenX software.

Preparation and Characterization of Nanoislands of LCO on Modified Substrates: Nanoislands of LCO were prepared on modified substrates with size of 25 mm² by utilizing a commercial self-ordered nanoporous anodic alumina (AAO) stencil mask with a diameter of ≈40 nm (Shenzhen Top-membranes Technology Co., Ltd). First, the AAO mask was attached to a clean LSAT substrate and subsequently grew a sacrificed SAO and an ultra-thin STO layer by PLD. Due to the high aspect ratio of the AAO mask, the thin film deposition process was performed at low oxygen pressures. After removing the AAO mask using a lift-off process, an array of STO/SAO nanoislands was left on the surface of the LSAT substrate. Next, the SAO layer was dissolved and transferred the FS-STO nanoislands to LAO substrates using thermally-release tape. Finally, LCO films were fabricated on the modified substrates under optimal growth conditions. A commercial scanning electron microscope (SEM, Hitachi, SU8200) was used to perform microscopic topography imaging.

Optical SHG Polarimetry: Optical SHG measurements were performed on an LCO hybrid homostructure with size of 25 mm². A focused 800 nm Ti: Sapphire femtosecond laser (Tsunami 3941-X1BB, Spectra-Physics) with a spot's diameter of 100 μm was incident at different regions of a LCO hybrid homostructure. The SHG signals were measured in the reflection geometry with incident angle of 45°. The second harmonic fields generated through the nonlinear optical process within LCO hybrid structures were decomposed into *p*-(*I_p* - *out*) and *s*-(*I_s* - *out*) polarized components by a beam splitter. The optical signals changed systematically with polarization direction (*φ*) of incident light. Then, the SHG polarimetry data were theoretically fitted with analytical models using standard point group symmetries.

STEM Imaging of Hybrid Structure: Cross-sectional TEM specimens of LCO hybrid structures were prepared using Ga⁺ ion milling after conventional mechanical thinning. The HAADF image were recorded in the scanning mode using JEM ARM 200CF microscopy at the Institute of Physics (IOP), Chinese Academy of Sciences (CAS). The sample was imaged from [100] zone axis of FS-STO membranes and LAO substrates. The atomic distances between A-cite elements were determined by fitting the intensity peaks using Gaussian function. The strain distribution within LCO hybrid structures were obtained using geometric pair analysis (GPA). All TEM data were analyzed using Gatan Digital Micrograph software.

Magnetic Characterizations: The macroscopic magnetization of LCO hybrid structures with size of 25 mm² were measured by a 7T-MPMS magnetometer. *M*-*T* curves were recorded during sample warm-up after field-cooled at 1 kOe. *M*-*H* loops were measured at 6 K by applying up to ± 7 T. The net magnetization of samples was obtained after subtracting diamagnetic signals from both FS-STO membranes and substrates. The evolution of magnetic domains was measured using a commercial cryogenic atomcubed MFM system. The hard magnetic coated point probes from Nano Sensor were used for scanning with a distance above the sample surface of ≈100 nm. Magnetic fields up to ± 2 T were applied perpendicular to the sample surface using superconducting magnet. All MFM measurements were conducted at 6 K to ensure LCO hybrid stays in ferromagnetic state. The diamond nitrogen vacancy (NV)-based magnetometry measurements were performed at zero magnetic field using a home-built optical detected magnetic resonance (ODMR) system. The nanodiamonds (ND) with a diameter of ≈100 nm were dispersed randomly on the surface of LCO hybrid structures. The ODMR signals were detected from LCO_T and LCO_C regions of an identical LCO hybrid sample separately by targeting an individual ND from corresponding regions using confocal microscopy. The measurements were taken by sweeping the microwave frequency through resonance and recording the optical excitation from an individual ND. The ODMR results were averaged over at least four measurements and double-checked at different NDs at the same region. The full ODMR spectrum exhibited a splitted two-peak-feature due to the Zeeman Effect and could be fitted using Lorentz function. The ODMR intensity changed systematically with sweeping microwave frequency. The LCO hybrid sample was cooled down to 6 K using a closure He-recycling refrigerator. The measurements were performed progressively during warm-up process from 6 to 150 K. After each measurement, the sample was thermally stabilized for an hour to achieve the accurate temperature.

XAS and XLD Measurements: Elemental specific XAS measurements were performed on LCO hybrid samples with size of 25 mm² grown on LAO substrates at the beamline 4B9B of the Beijing Synchrotron Radiation Facility (BSRF). All spectra at both O *K*-edges and Co *L*-edges were collected at room temperature in total electron yield (TEY) mode. The LCO hybrid structures were properly grounded using copper tapes to obtain the best signal-to-noise ratio. The typical photocurrents measured using TEY mode were in the order of pA. XAS measurements were performed alternately at LCO_C and LCO_T regions of LCO hybrid structures. The incident angles of linearly polarized X-ray beam vary from 90° to 30° with respect to the surface plane. When the incident angle sets to 90°, XAS signals reflects the *d_{x²-y²}* orbital occupancy directly, whereas the incident angle changes to 30°, XAS contains both *d_{x²-y²}* and *d_{3z²-r²}* orbital information. To quantify the orbital occupancy in Co *e_g* bands, the nominal XLD by *I_{90°}* - *I_{30°}* was calculated. All XAS data were normalized to the values at the pre- and post-edges for direct comparison.

Statistical Analysis: The size of substrates was indicated in each measurement sections. For the magnetization measurements, the magnetic hysteresis loops were obtained by subtracting the linear diamagnetic signals from the original data. For XAS and XLD data, the spectra were normalized to its pre- and post-peaks following the standard data processing procedure. For STEM, SEM, and MFM data, no additional process was needed. The data were processed using Origin software. For STEM and SEM images, Gatan DigitalMicrograph software was used.

Supporting Information

Supporting Information is available from the Wiley Online Library or from the author.

Acknowledgements

The authors sincerely thank to the assistance and guidance on AAO mask fabrication from X.G. at South China Normal University. The authors thank to T.G. at SLAB for the extensive assistance in magnetization measurements. This work was supported by the National Key Basic Research Program of China (grant nos. 2020YFA0309100 and 2019YFA0308500), the National Natural Science Foundation of China (grant nos. 11974390, U22A20263, 52250308, 11721404, 12174364, 11874412, 52072400, 52025025, and 12174347), the Guangdong-Hong Kong-Macao Joint Laboratory for Neutron Scattering Science and Technology, and the Strategic Priority Research Program (B) of the Chinese Academy of Sciences (grant no. XDB33030200). Synchrotron-based XRD measurements were performed at the beamline 1W1A and XAS and XLD experiments were performed at the beamline 4B9B of the Beijing Synchrotron Radiation Facility (BSRF) via user proposals.

Conflict of Interest

The authors declare no conflict of interest.

Author Contributions

S.C. and D.R. contributed equally to this work. The freestanding STO layers and LCO hybrid samples were grown and processed by S.R.C.; the transfer of freestanding oxide membranes was conducted by D.K.R.; Temperature dependent NV magnetometry was performed by Y.X. and Y.X.S. under guidance of G.Q.L.; MFM images were recorded by M.M.C. under guidance of J.X.Z.; SHG measurements were carried out by S.X. under guidance of K.J.J.; XAS and XLD measurements were performed by S.R.C., H.T.H., T.C., Q.J., and J.O.W.; TEM lamellas were fabricated with FIB milling and TEM experiments were performed by X.Y.L., Q.H.Z., and L.G.; S.R.C., D.K.R., T.C., Q.J., and H.T.H. worked on the structural and magnetic measurements. C.W. and H.G. participated the discussions and K.J.J. provided important suggestions during the manuscript preparation. E.J.G. initiated the research and supervised the work. S.R.C. and E.J.G. wrote the manuscript with inputs from all authors.

Data Availability Statement

The data that support the findings of this study are available from the corresponding author upon reasonable request.

Keywords

cobaltites, data storage bit, magnetic domains, morphotropic homostructures, spin state transitions

Received: March 15, 2023

Revised: April 18, 2023

Published online:

- [1] S. N. Piramanayagam, T. C. Chong, *Developments in Data Storage*, IEEE-Wiley, Press, Piscataway, NJ **2012**.
- [2] A. von Reppert, L. Willig, J.-E. Pudell, S. P. Zeuschner, G. Sellge, F. Ganss, O. Hellwig, J. A. Arregi, V. Uhlir, A. Crut, M. Bargheer, *Sci. Adv.* **2020**, *6*, eaba1142.
- [3] A. Singh, S. Mukhopadhyay, A. Ghosh, *Phys. Rev. Lett.* **2010**, *105*, 067206.
- [4] E. Berganza, M. Jaafar, J. A. Fernandez-Roldan, M. Goiriena-Goikoetxea, J. Pablo-Navarro, A. Garcia-Arribas, K. Gusliencko, C. Magén, J. M. De Teresa, O. Chubykalo-Fesenko, A. Asenjo, *Nanoscale* **2020**, *12*, 18646.
- [5] D. E. J. Waddington, T. Boele, R. Maschmeyer, Z. Kuncic, M. S. Rosen, *Sci. Adv.* **2020**, *6*, eabb0998.
- [6] M. Mallary, A. Torabi, M. Benakli, *IEEE Trans. Magn.* **2002**, *38*, 1719.
- [7] C. Vogler, C. Abert, F. Bruckner, D. Suess, D. Praetorius, *Appl. Phys. Lett.* **2016**, *108*, 102406.
- [8] J. Mannhart, D. G. Schlom, *Science* **2010**, *327*, 1607.
- [9] D. Kan, R. Aso, R. Sato, M. Haruta, H. Kurata, Y. Shimakawa, *Nat. Mater.* **2016**, *15*, 432.
- [10] Z. Liao, M. Huijben, Z. Zhong, N. Gauquelin, S. Macke, R. J. Green, S. Van Aert, J. Verbeeck, G. Van Tendeloo, K. Held, G. A. Sawatzky, G. Koster, G. Rijnders, *Nat. Mater.* **2016**, *15*, 425.
- [11] S. Lin, Q. H. Zhang, M. A. Roldan, S. Das, T. Charlton, M. R. Fitzsimmons, Q. Jin, S. S. Li, Z. P. Wu, S. Chen, H. Z. Guo, X. Tong, M. He, C. Ge, C. Wang, L. Gu, K. J. Jin, E. J. Guo, *Phys. Rev. Appl.* **2020**, *13*, 034033.
- [12] J. Zhang, Z. C. Zhong, X. X. Guan, X. Shen, J. E. Zhang, F. R. Han, H. Zhang, H. R. Zhang, X. Yan, Q. H. Zhang, L. Gu, F. X. Hu, R. C. Yu, B. G. Shen, J. R. Sun, *Nat. Commun.* **2018**, *9*, 1923.
- [13] S. Thomas, B. Kuiper, J. Hu, J. Smit, Z. Liao, Z. Zhong, G. Rijnders, A. Vailionis, R. Wu, G. Koster, J. Xia, *Phys. Rev. Lett.* **2017**, *119*, 117203.
- [14] D. Fuchs, C. Pinta, T. Schwarz, P. Schweiss, P. Nagel, S. Schuppler, R. Schneider, M. Merz, G. Roth, H. V. Löhneysen, *Phys. Rev. B* **2007**, *75*, 144402.
- [15] V. V. Mehra, N. Biskup, C. Jenkins, E. Arenholz, M. Varela, Y. Suzuki, *Phys. Rev. B* **2015**, *91*, 144418.
- [16] W. S. Choi, J. H. Kwon, H. Jeon, J. E. Hamann-Borrero, A. Radi, S. Macke, R. Sutarto, F. He, G. A. Sawatzky, V. Hinkov, M. Kim, H. N. Lee, *Nano Lett.* **2012**, *12*, 4966.
- [17] R. J. Zeches, M. D. Rossell, J. X. Zhang, A. J. Hatt, Q. He, C.-H. Yang, A. Kumar, C. H. Wang, A. Melville, C. Adamo, G. Sheng, Y.-H. Chu, J. F. Ihlefeld, R. Erni, C. Ederer, V. Gopalan, L. Q. Chen, D. G. Schlom, N. A. Spaldin, L. W. Martin, R. Ramesh, *Science* **2009**, *326*, 977.
- [18] A. Herklotz, M. D. Biegalski, H. S. Kim, L. Schultz, K. Dorr, H. M. Christen, *New J. Phys.* **2010**, *12*, 113053.
- [19] P. C. Wu, C. C. Wei, Q. L. Zhong, S. Z. Ho, Y. D. Liou, Y. C. Liu, C. C. Chiu, W. Y. Tzeng, K. E. Chang, Y. W. Chang, J. D. Zheng, C. F. Chang, C. M. Tu, T. M. Chen, C. W. Luo, R. Huang, C. G. Duan, Y. C. Chen, C. Y. Kuo, J. C. Yang, *Nat. Commun.* **2022**, *13*, 2565.
- [20] S. R. Chen, Q. H. Zhang, D. K. Rong, Y. Xu, J. F. Zhang, F. F. Pei, H. Bai, Y. X. Shang, S. Lin, Q. Jin, H. T. Hong, C. Wang, W. S. Yan, H. Z. Guo, T. Zhu, L. Gu, Y. Gong, Q. Li, L. F. Wang, G. Q. Liu, K. J. Jin, E. J. Guo, *Adv. Mater.* **2023**, *35*, 2206961.
- [21] D. Lu, D. J. Baek, S. S. Hong, L. F. Kourkoutis, Y. Hikita, H. Y. Hwang, *Nat. Mater.* **2016**, *15*, 1255.
- [22] J. H. Kwon, W. S. Choi, Y. K. Kwon, R. Jung, J. M. Zuo, H. N. Lee, J. Kim, *Chem. Mater.* **2014**, *26*, 2496.
- [23] E. J. Guo, R. Desautels, D. Lee, M. A. Roldan, Z. L. Liao, T. Charlton, H. Ambaye, J. Molaison, R. Boehler, D. Keavney, A. Herklotz, T. Z. Ward, H. N. Lee, M. R. Fitzsimmons, *Phys. Rev. Lett.* **2019**, *122*, 187202.
- [24] E. J. Guo, R. Desautels, D. Keavnet, M. A. Roldan, B. J. Kirby, D. Lee, Z. L. Liao, T. Charlton, A. Herklotz, T. Z. Ward, M. R. Fitzsimmons, H. N. Lee, *Sci. Adv.* **2019**, *5*, eaav5050.
- [25] V. M. Acosta, E. Bauch, M. P. Ledbetter, A. Waxman, L. S. Bouchard, D. Budker, *Phys. Rev. Lett.* **2010**, *104*, 070801.
- [26] Z. Hu, H. Wu, M. W. Haverkort, H. H. Hsieh, H.-J. Lin, T. Lorenz, J. Baier, A. Reichl, I. Bonn, C. Felser, A. Tanaka, C. T. Chen, L. H. Tjeng, *Phys. Rev. Lett.* **2004**, *92*, 207402.
- [27] M. W. Haverkort, Z. Hu, J. C. Cezar, T. Burnus, H. Hartmann, M. Reuther, C. Zobel, T. Lorenz, A. Tanaka, N. B. Brookes, H. H. Hsieh, H.-J. Lin, C. T. Chen, L. H. Tjeng, *Phys. Rev. Lett.* **2006**, *97*, 176405.
- [28] W. Lee, R. Ji, U. Gösele, K. Nielsch, *Nat. Mater.* **2006**, *9*, 741.
- [29] W. Lee, H. Han, A. Lotnyk, M. A. Schubert, S. Senz, M. Alexe, D. Hesse, S. Baik, U. Gösele, *Nat. Nanotechnol.* **2008**, *3*, 402.
- [30] G. Tian, F. Zhang, J. Yao, H. Fan, P. Li, Z. Li, X. Song, X. Zhang, M. Qin, M. Zeng, Z. Zhang, J. Yao, X. Gao, J. Liu, *ACS Nano* **2016**, *10*, 1025.
- [31] Z. W. Li, Y. J. Wang, G. Tian, P. L. Li, L. Zhao, F. Y. Zhang, J. X. Yao, H. Fan, X. Song, D. Y. Chen, Z. Fan, M. H. Qin, M. Zeng, Z. Zhang, X. B. Lu, S. J. Hu, C. H. Lei, Q. F. Zhu, J. Y. Li, X. S. Gao, J. M. Liu, *Sci. Adv.* **2017**, *3*, e1700919.
- [32] *Pulsed Laser Deposition of Thin Films (Applications-LED Growth of Functional Materials)* (Ed.: R Eason), Wiley-Interscience John Wiley & Sons, Inc., Hoboken, NJ **2007**.
- [33] *Thin Films and Heterostructures for Oxide Electronics* (Ed.: S B. Ogale), Springer Science+Business Media Inc., Berlin, Germany **2005**.
- [34] E. J. Guo, R. D. Desautels, D. Keavney, A. Herklotz, T. Z. Ward, M. R. Fitzsimmons, H. N. Lee, *Phys. Rev. Mater.* **2019**, *3*, 014407.
- [35] M. Huijben, L. W. Martin, Y. H. Chu, M. B. Holcomb, P. Yu, G. Rijnders, D. H. A. Blank, R. Ramesh, *Phys. Rev. B* **2008**, *78*, 094413.
- [36] H. Zheng, J. Wang, S. E. Lofland, Z. Ma, L. Mahaddes-Ardabili, T. Zhao, L. Salamanca-Riba, S. R. Shinde, S. B. Ogale, F. Bai, D. Viehland, Y. Jia, D. G. Schlom, M. Wuttig, A. Roytburd, R. Ramesh, *Science* **2004**, *303*, 661.
- [37] M. A. Gilleo, S. Geller, *Phys. Rev.* **1958**, *110*, 73.
- [38] J. Seidel, L. W. Martin, Q. He, Q. Zhan, Y. H. Chu, A. Rother, M. E. Hawkrigge, P. Maksymovych, P. Yu, M. Gajek, N. Balke, S. V. Kalinin, S. Gemming, F. Wang, G. Catalan, J. F. Scott, N. A. Spaldin, J. Orenstein, R. Ramesh, *Nat. Mater.* **2009**, *8*, 229.
- [39] J. Ma, J. Ma, Q. Zhang, R. Peng, J. Wang, C. Liu, M. Wang, N. Li, M. Chen, X. Cheng, P. Gao, L. Gu, L.-Q. Chen, P. Yu, J. Zhang, C.-W. Nan, *Nat. Nanotechnol.* **2018**, *13*, 947.
- [40] Y. Cao, V. Fatemi, A. Demir, S. Fang, S. L. Tomarken, J. Y. Luo, J. D. Sanchez-Yamagishi, K. Watanabe, T. Taniguchi, E. Kaxiras, R. C. Ashoori, P. Jarillo-Herrero, *Nature* **2018**, *556*, 80.